Electronic Supplementary Information (ESI) for Nanoscale

A General Strategy for Tailoring Upconversion Luminescence in Lanthanide-Doped Inorganic Nanocrystals through Local Structure Engineering

Huhui Fu,[abcd] Pengfei Peng,[ac] Renfu Li,[a] Caiping Liu,[a] Yongsheng Liu,[*ab] Feilong Jiang,[a] Maochun Hong,[*abc] Xueyuan Chen[*abc]

[a]CAS Key Laboratory of Design and Assembly of Functional Nanostructures, and State Key Laboratory of Structural Chemistry, Fujian Institute of Research on the Structure of Matter, Chinese Academy of Sciences, Fuzhou, Fujian 350002, China.

[b]University of the Chinese Academy of Sciences, Beijing, 100049, China

[c]School of Physical Science and Technology, ShanghaiTech University, Shanghai 201210, China

[d]Shanghai Institute of Ceramics, Chinese Academy of Sciences, Shanghai 200050, China

*To whom correspondence should be addressed, e-mail: liuysh@fjirsm.ac.cn, hmc@fjirsm.ac.cn, and xchen@fjirsm.ac.cn

Supplementary Experimental Section

General procedure for the Preparation of $NaYF_4$:Yb/Er nanocrystals (NCs). In a typical procedure of the synthesis of hexagonal-phase $NaYF_4$:Yb/Er nanocrystals, 0.39 mmol of $Y(CH_3CO_2)_3.4H_2O$, 0.1 mmol of $Yb(CH_3CO_2)_3.4H_2O$ and 0.01 mmol of $Er(CH_3CO_2)_3.4H_2O$ were mixed with 5 mL of oleic acid (OA) and 16 mL of 1-octadecene (ODE) in a 100 mL three-neck round-bottom flask. The solution was heated to 150 °C under N_2 flow with constant stirring for 60 min to form a clear solution, and then cooled down to room temperature. Thereafter, 10 mL of methanol solution containing 1.25 mmol of NaOH and 2 mmol of NH_4F was added and the resulting mixture was stirred for 30 min. After removal of the methanol by evaporation, the solution was heated to 300 °C under N_2 flow with vigorous stirring for 60 min, and then cooled down to room temperature. The resulting hexagonal-phase $NaYF_4$:Yb/Er NCs were precipitated by addition of ethanol, collected by centrifugation, washed with ethanol for several times, and finally re-dispersed in cyclohexane. The synthetic procedure for the cubic-phase $NaYF_4$:Yb/Er NCs was the same as that used to synthesize the hexagonal-phase $NaYF_4$:Yb/Er NCs, except that the amount of NaOH and reaction temperature were changed to 0.5 mmol and 270 °C, respectively.

Supplementary Tables

Table S1. Comparison of the optimized crystal lattice parameters by using the first-principle calculation based on density functional theory (DFT) for Yb^{3+}, Er^{3+} and Yb^{3+}/ Er^{3+} doped Na_3ZrF_7, $Na_5Zr_2F_{13}$ and $Na_7Zr_6F_{31}$ crystals with the experimental data of their pure counterparts from JCPDS or ICSD database.

	Na_3ZrF_7[a]	**Na_3ZrF_7:Er**	**Na_3ZrF_7:Yb**	**Na_3ZrF_7:Yb/Er**
Space group	*I*4/*mmm*	*I*4/*mmm*	*I*4/*mmm*	*I*4/*mmm*
a / Å	10.4264	10.4312	10.3954	10.4032
b / Å	10.4264	10.4312	10.3954	10.4032
c / Å	10.5126	10.5361	10.5114	10.5158
α	90.000	90.000	90.000	90.000
β	90.000	90.000	90.000	90.000
γ	90.000	90.000	90.000	90.000
V / Å^3	1142.808	1146.43	1135.91	1138.10
	$Na_5Zr_2F_{13}$[a]	**$Na_5Zr_2F_{13}$:Er**	**$Na_5Zr_2F_{13}$:Yb**	**$Na_5Zr_2F_{13}$:Yb/Er**
Space group	*C*2/*m*	*C*2/*m*	*C*2/*m*	*C*2/*m*
a / Å	11.5475	11.5592	11.5512	11.5582
b / Å	11.1066	11.1093	10.9870	10.9965
c / Å	8.9122	8.9409	8.9251	8.9548
α	90.000	90.000	90.000	90.000
β	93.216	93.101	93.074	92.922
γ	90.000	90.000	90.000	90.000
V / Å^3	1141.23	1146.46	1131.09	1136.67
	$Na_7Zr_6F_{31}$[a]	**$Na_7Zr_6F_{31}$:Er**	**$Na_7Zr_6F_{31}$:Yb**	**$Na_7Zr_6F_{31}$:Yb/Er**
Space group	*R*-3	*R*-3	*R*-3	*R*-3
a / Å	13.4617	13.5717	13.5573	13.5905
b / Å	13.4617	13.5411	13.5411	13.5969
c / Å	9.3850	9.3662	9.3883	9.4163
α	90.000	89.982	89.952	90.104
β	90.000	89.985	89.956	89.991
γ	120.000	120.339	120.215	120.350
V / Å^3	1472.87	1485.55	1489.35	1501.56

[a]The calculated crystal lattice parameters for pure tetragonal-phase Na_3ZrF_7, monoclinic-phase $Na_5Zr_2F_{13}$, trigonal-phase $Na_7Zr_6F_{31}$ crystals are well consistent with the experimental crystal lattice parameters reported from JCPDS or ICSD database (JCPDS No. 12-0562 for Na_3ZrF_7, ICSD No. 155759 for $Na_5Zr_2F_{13}$ and JCPDS No. 72-1551 for $Na_7Zr_6F_{31}$), which thereby demonstrates the reliability of our first-principle calculation based on DFT.

Table S2. Calculated formation energies (defined as the energy difference per unit cell between the nanocrystal and isolated atoms) for pure, Yb^{3+}, Er^{3+} and Yb^{3+}/Er^{3+} doped Na_3ZrF_7, $Na_5Zr_2F_{13}$ and $Na_7Zr_6F_{31}$ crystals by using the first-principle calculation based on DFT. Generally speaking, the larger absolute value of formation energy, the more stable is the crystal.

Crystal	Content of dopant (mol %)	Formation energy per atom (eV)
Na_3ZrF_7	0	-64.11
Na_3ZrF_7:Er	12.5	-64.12
Na_3ZrF_7:Yb	12.5	-64.26
Na_3ZrF_7:Yb/Er	12.5 (Yb/Er = 1)	-64.26
$Na_5Zr_2F_{13}$	0	-4.13
$Na_5Zr_2F_{13}$:Er	12.5	-4.14
$Na_5Zr_2F_{13}$:Yb	12.5	-4.30
$Na_5Zr_2F_{13}$:Yb/Er	12.5 (Yb/Er = 1)	-4.31
$Na_7Zr_6F_{31}$	0	-19.35
$Na_7Zr_6F_{31}$:Er	12.5	-19.36
$Na_7Zr_6F_{31}$:Yb	12.5	-19.43
$Na_7Zr_6F_{31}$:Yb/Er	12.5 (Yb/Er = 1)	-19.43

Table S3. Actual Yb^{3+} and Er^{3+} doping concentrations determined form the inductively coupled plasma atomic emission spectroscopy (ICP-AES) for Na_3ZrF_7:Yb/Er, $Na_5Zr_2F_{13}$:Yb/Er and $Na_7Zr_6F_{31}$:Yb/Er NCs doped with 20 mol% Yb^{3+} and 2 mol% Er^{3+}.

Sample	Nominal Yb/Er doping content (mol%)	Actual Yb/Er doping content from ICP-AES (mol%)
Na_3ZrF_7:Yb/Er	20/2	19.8 ± 1.1/1.9 ± 0.2
$Na_5Zr_2F_{13}$:Yb/Er	20/2	18.6 ± 0.9/2.1 ± 0.3
$Na_7Zr_6F_{31}$:Yb/Er	20/2	20.1 ± 1.6/1.8 ± 0.3

Supplementary Figures

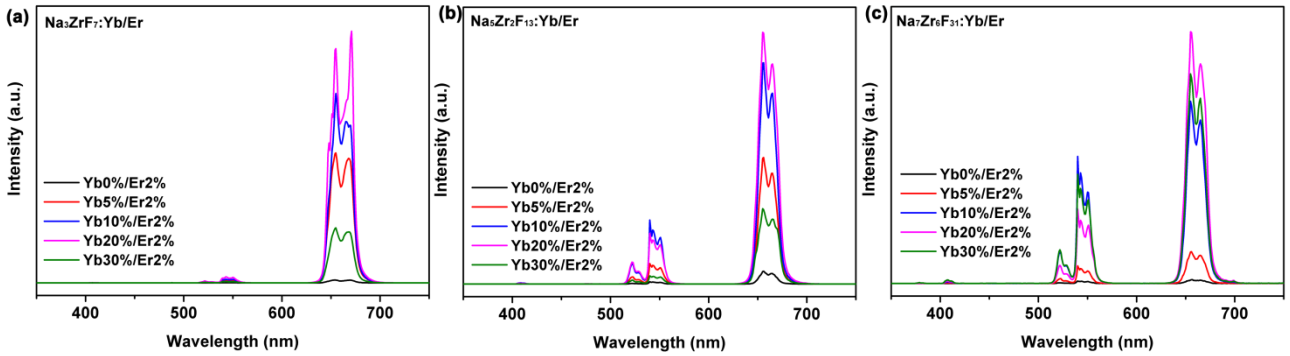

Figure S1. Room-temperature UC luminescence (UCL) spectra for a series of Yb/Er co-doped Na_3ZrF_7, $Na_5Zr_2F_{13}$ and $Na_7Zr_6F_{31}$ NCs as a function of the Yb^{3+} ion doping concentration. All the UCL spectra were measured under identical experimental conditions upon a 980-nm diode laser excitation with a power density of 30 W cm^{-2}. These results clearly demonstrate that the optimum Yb^{3+} doping concentration for intense UCL of Er^{3+} was 20 mol% in Na_3ZrF_7, $Na_5Zr_2F_{13}$ and $Na_7Zr_6F_{31}$ NCs, respectively.

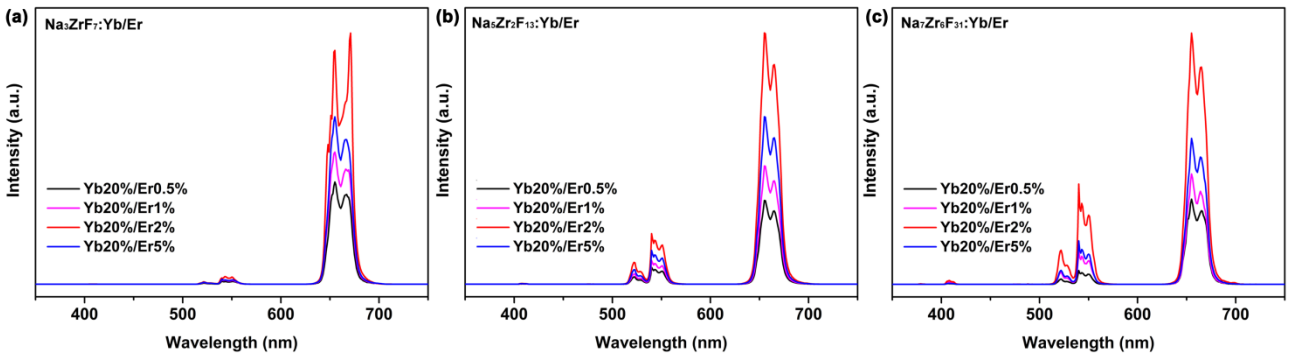

Figure S2. Room-temperature UCL spectra for a series of Yb/Er co-doped Na_3ZrF_7, $Na_5Zr_2F_{13}$ and $Na_7Zr_6F_{31}$ NCs as a function of the Er^{3+} ion doping concentration. All the UCL spectra were measured under identical experimental conditions upon a 980-nm diode laser excitation with a power density of 30 W cm^{-2}. These results clearly show that the optimum Er^{3+} doping concentration for intense UCL was determined to be 2 mol% in Na_3ZrF_7, $Na_5Zr_2F_{13}$ and $Na_7Zr_6F_{31}$ NCs, respectively.

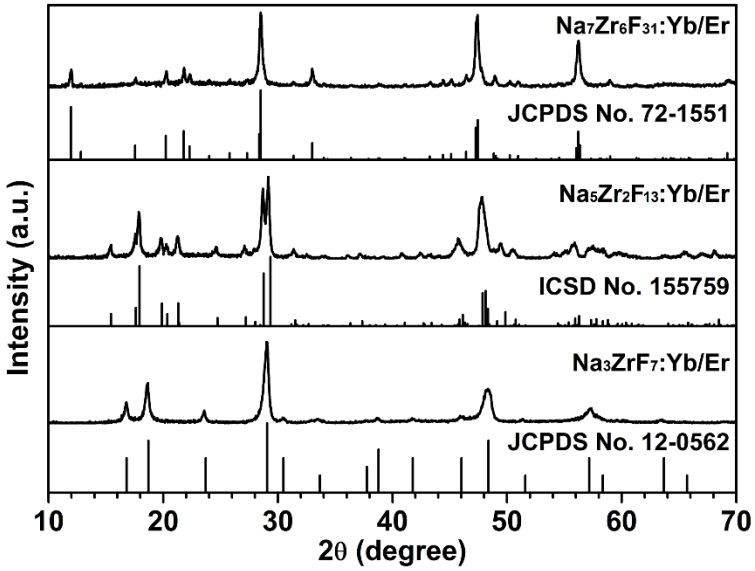

Figure S3. Powder X-ray diffraction (XRD) patterns for the as-synthesized Yb^{3+}/Er^{3+} (20/2 mol%) co-doped Na_3ZrF_7, $Na_5Zr_2F_{13}$ and $Na_7Zr_6F_{31}$ NCs, showing that all the XRD peaks can be well indexed in accordance with tetragonal-phase Na_3ZrF_7 structure (JCPDS No. 12-0562,space group *I*4/mmm), monoclinic-phase $Na_5Zr_2F_{13}$ structure (ICSD No. 155759, space group *C*2/m) and trigonal-phase $Na_7Zr_6F_{31}$ structure (JCPDS No. 72-1551, space group *R*-3), respectively.

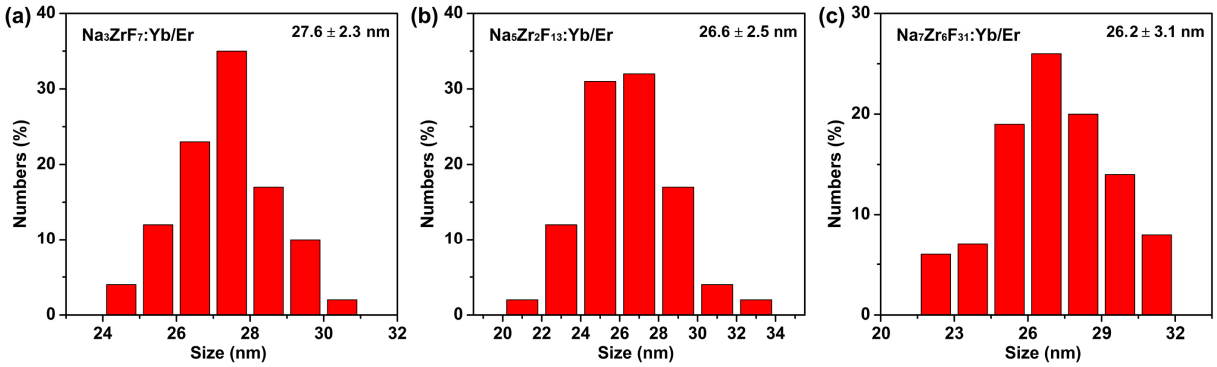

Figure S4. Size distributions for the as-synthesized Yb^{3+}/Er^{3+} co-doped a) Na_3ZrF_7, b) $Na_5Zr_2F_{13}$ and c) $Na_7Zr_6F_{31}$ NCs. The average sizes for the as-synthesized Yb^{3+}/Er^{3+} co-doped Na_3ZrF_7, $Na_5Zr_2F_{13}$ and $Na_7Zr_6F_{31}$ NCs were determined to be 27.6 ± 2.3, 26.6 ± 2.5 and 26.2 ± 3.1 nm, respectively, on the basis of their corresponding size histograms obtained from TEM images of 200 nanocrystals.

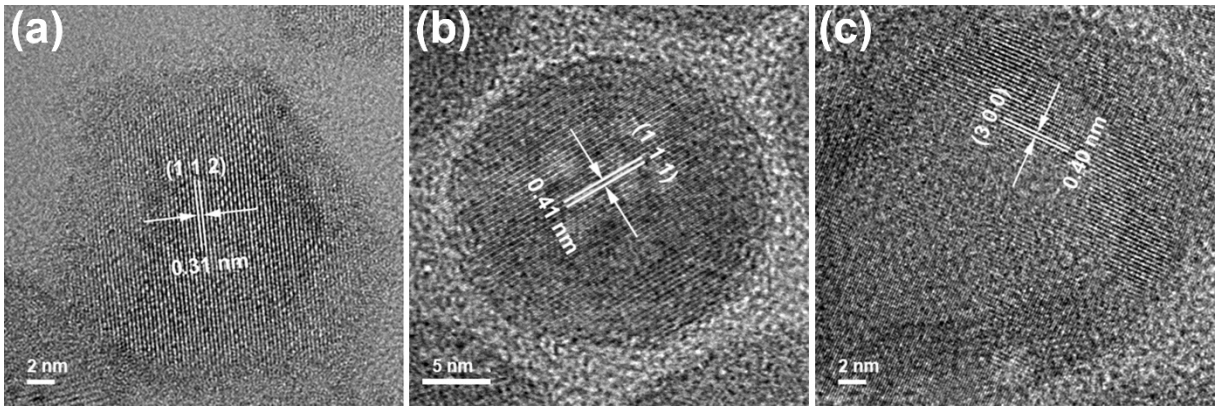

Figure S5. High-resolution transmission electron microscopy (TEM) images for the as-synthesized a) Na_3ZrF_7:Yb/Er, b) $Na_5Zr_2F_{13}$:Yb/Er and c) $Na_7Zr_6F_{31}$:Yb/Er NCs. The high-resolution TEM images show lattice fringes with observed d-spacing of 0.31, 0.41 and 0.40 nm, which are in good agreement with the lattice spacings of the (112), (111) and (300) planes for tetragonal-phase Na_3ZrF_7, monoclinic-phase $Na_5Zr_2F_{13}$ and trigonal-phase $Na_7Zr_6F_{31}$ crystals, respectively, and then demonstrate the high crystallinity for the as-synthesized Na_3ZrF_7:Yb/Er, $Na_5Zr_2F_{13}$:Yb/Er and $Na_7Zr_6F_{31}$:Yb/Er NCs.

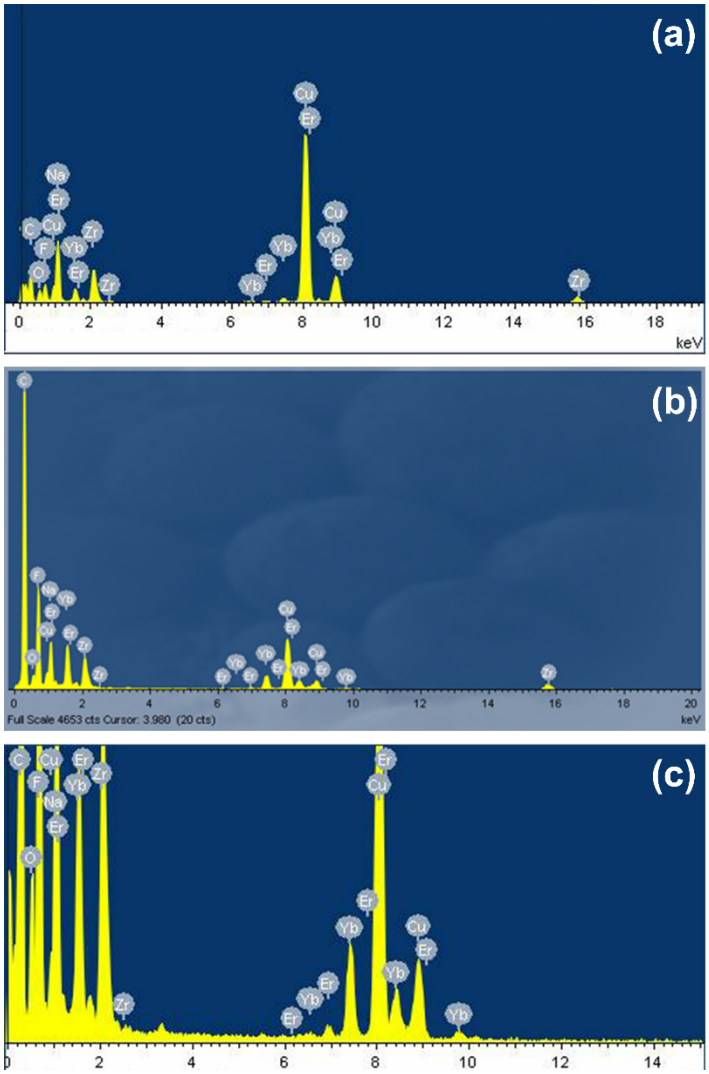

Figure S6. Energy-dispersive X-ray spectroscopy (EDS) analyses for the as-synthesized Na_3ZrF_7:Yb/Er, b) $Na_5Zr_2F_{13}$:Yb/Er and c) $Na_7Zr_6F_{31}$:Yb/Er NCs, revealing the presence of the doped elements of Yb and Er in all the as-synthesized NCs.

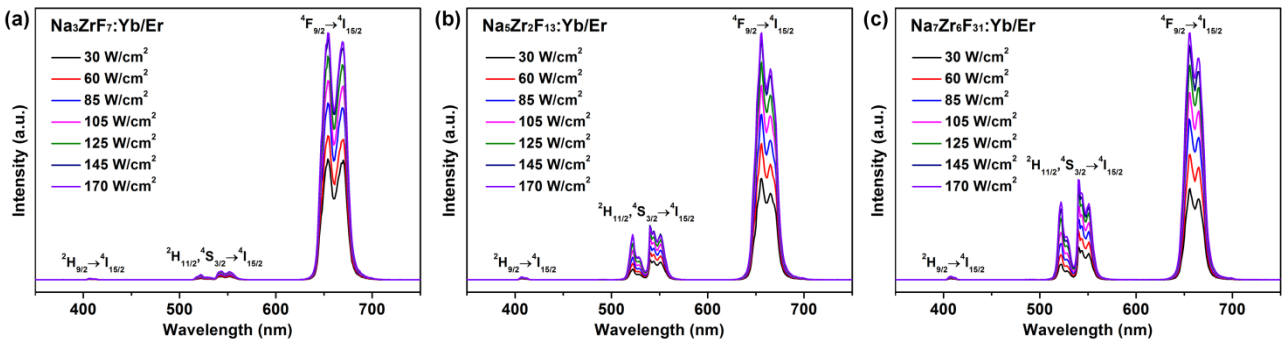

Figure S7. Room-temperature UCL spectra for Yb/Er (20/2 mol%) co-doped a) Na_3ZrF_7, b) $Na_5Zr_2F_{13}$ and c) $Na_7Zr_6F_{31}$ NCs as a function of the varied excitation power density of 980-nm diode laser. The UCL peaks ascribed to the $^2H_{9/2}\rightarrow{}^4I_{15/2}$ transition of Er^{3+} for Yb/Er (20/2 mol) co-doped Na_3ZrF_7, $Na_5Zr_2F_{13}$ and $Na_7Zr_6F_{31}$ NCs were hardly detectable even at a high power density of excitation of 980-nm diode laser up to 170 W cm^{-2}. These results indicate that the populations of high-lying energy levels (e.g., $^2H_{9/2}$ and $^2H_{11/2}$) of Er^{3+} involving a large number of UC excitation steps in these NCs is strongly suppressed particularly for the Na_3ZrF_7:Yb/Er NCs with high-symmetry local structure of host Zr^{4+} ion.

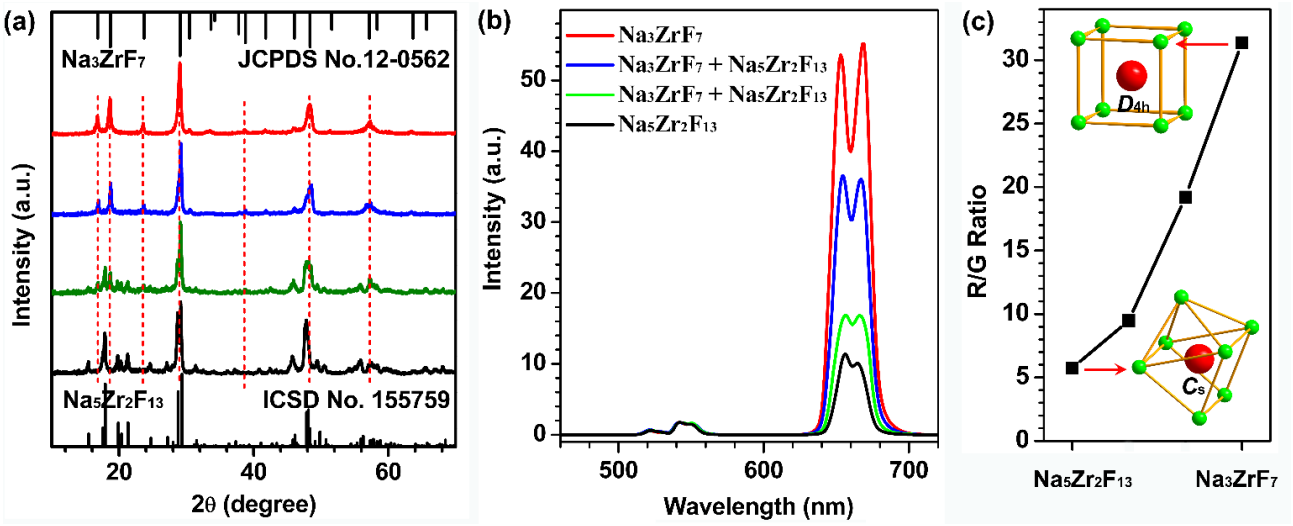

Figure S8. a) XRD patterns for the mixed sodium zirconium fluoride NCs with different Na_3ZrF_7:Yb/Er and $Na_5Zr_2F_{13}$:Yb/Er contents and their corresponding b) UCL patterns and c) UCL red-to-green (R/G) intensity ratios with the varied site symmetries of host Zr^{4+} ion. Note that all the UCL patterns in Figure S8b were normalized at the green UCL band centered at 542 nm to clearly demonstrate the evolution of the R/G intensity ratio with the gradually increased $Na_5Zr_2F_{13}$:Yb/Er content. The transformation from tetragonal-phase Na_3ZrF_7 to monoclinic-phase $Na_5Zr_2F_{13}$ crystal structure in these mixed NCs can be well evidenced by using the XRD analysis (Figure S8a). As a result, the R/G UCL ratio in these samples was observed to dramatically decrease (Figure S8b-c) with the increasing content of $Na_5Zr_2F_{13}$:Yb/Er NCs with C_s site-symmetry of host Zr^{4+} ion, which unambiguously demonstrates the critical role of local structure (or site symmetry) of host Zr^{4+} ion in regulating the UCL profiles for the doped Er^{3+} ion.

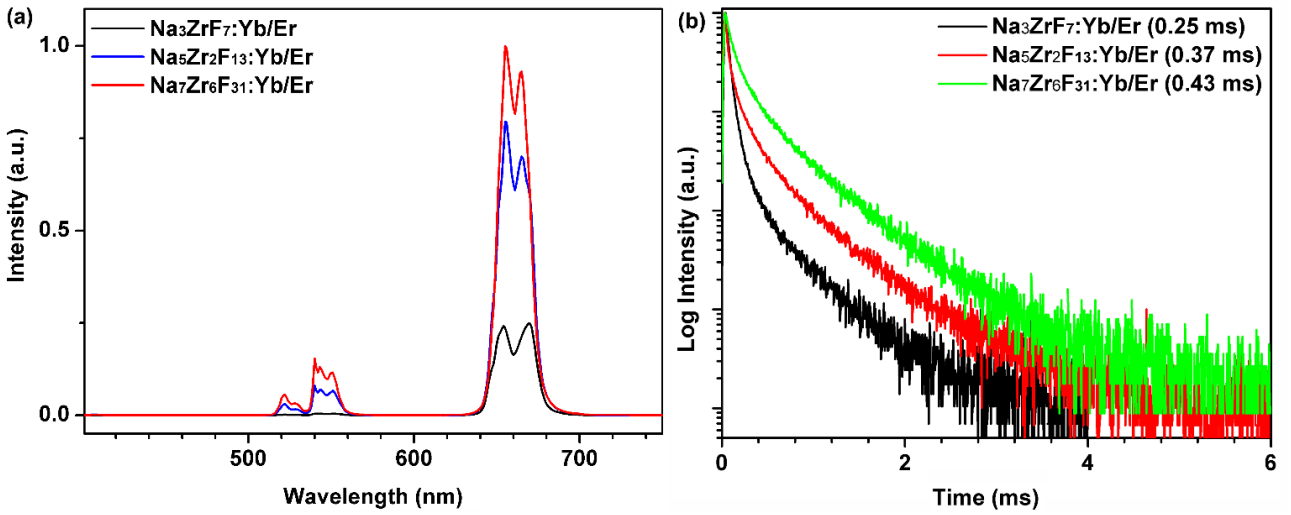

Figure S9. Comparison of a) UCL spectra and b) decay curves for Yb/Er (20/2 mol%) co-doped Na_3ZrF_7, $Na_5Zr_2F_{13}$ and $Na_7Zr_6F_{31}$ NCs. Note that all the UCL spectra were measured under identical experimental conditions upon a 980-nm diode laser excitation with a power density of 30 W cm^{-2}, while the UCL decay curves were collected by monitoring Er^{3+} UCL centered at 650 nm upon excitation by a 980-nm pulsed laser. The integrated UCL intensity for Yb^{3+}/Er^{3+} co-doped Na_3ZrF_7 NCs was found to be about 3-5 times weaker than those in $Na_5Zr_2F_{13}$:Yb/Er and $Na_7Zr_6F_{31}$:Yb/Er counterparts, and the effective UCL lifetime of Er^{3+} ion in Na_3ZrF_7:Yb/Er NCs was also determined to be shorter than those in $Na_5Zr_2F_{13}$:Yb/Erand $Na_7Zr_6F_{31}$:Yb/Er NCs. The weaker UCL intensity and shorter UCL lifetime for Yb/Er co-doped Na_3ZrF_7 NCs is understandable due to the high-symmetry two-dimensional layered sublattice of Zr^{4+} ion that facilitates the long-distance energy transfer between the doping Er^{3+} (or Yb^{3+}) ions and their neighboring Zr^{4+} ions (or lattice/surface defects) and thus promote the dissipation of the excitation energy as heat in the lattices of Na_3ZrF_7 NCs.

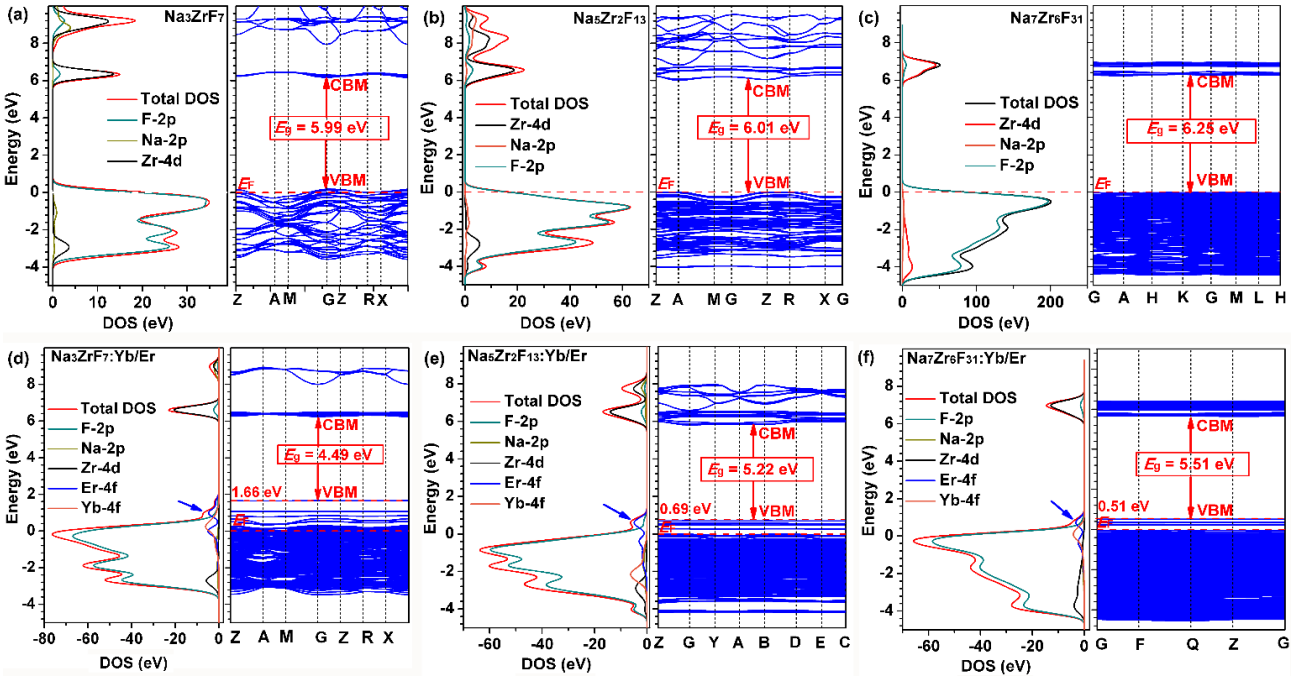

Figure S10. Comparison of DFT-calculated electronic band structures (right) and projected density of states (DOS) (left) for a-c) pure and d-f) Yb/Er co-doped Na_3ZrF_7, $Na_5Zr_2F_{13}$ and $Na_7Zr_6F_{31}$ NCs. Note that the Eg represents the band gap energy between the conduction band minimum (CBM) and the valence band maximum (VBM), and the and EF represents the Fermi level (0 eV) of sodium zirconium fluoride NCs. These DFT calculations show that the VBM for all the NCs is mainly contributed by the F 2p-orbitals, whereas the CBM originates predominately from the Zr 4d-orbitals. The band gap energies for Yb/Er co-doped Na_3ZrF_7, $Na_5Zr_2F_{13}$ and $Na_7Zr_6F_{31}$ NCs were calculated to be 4.49, 5.22 and 5.51 eV, respectively, much smaller than those of their pure counterparts (5.99, 6.01 and 6.25 eV for Na_3ZrF_7, $Na_5Zr_2F_{13}$ and $Na_7Zr_6F_{31}$ NCs, respectively). More importantly, the VBM for Na_3ZrF_7:Yb/Er NCs was calculated to significantly increase from Fermi level (EF, 0 eV) to 1.66 eV, much higher than the incremental values achieved in the $Na_5Zr_2F_{13}$:Yb/Er (~0.69 eV) and $Na_7Zr_6F_{31}$:Yb/Er (~0.51 eV) NCs. These results clearly demonstrate that the symmetry of crystal lattice of these Yb/Er co-doped Na_3ZrF_7, $Na_5Zr_2F_{13}$ and $Na_7Zr_6F_{31}$ NCs has significant impact on their respective electronic band structures upon doping of Yb^{3+} and Er^{3+} as well as the UCL behaviors of lanthanide emitters.

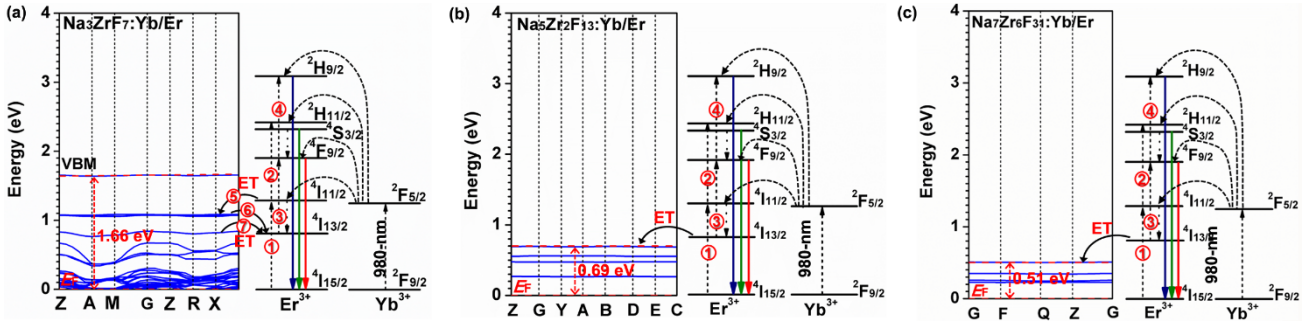

Figure S11. DFT-calculated electronic band structures (left) and the proposed energy transfer (ET) mechanisms between the excited Yb^{3+}, Er^{3+} and the valence bands in a) Na_3ZrF_7:Yb/Er, $Na_5Zr_2F_{13}$:Yb/Er and $Na_7Zr_6F_{31}$:Yb/Er NCs following excitation with a 980-nm laser. Note that the dashed, dotted, black and colored full arrows represent photon excitation, non-radiative multiphonon relaxation, ET and emission processes, respectively. Benefitting from the significantly increased VBM (1.66 eV) coupled with the unique electronic structure of Na_3ZrF_7:Yb/Er NCs, the ET steps marked by 5 to 7 in Figure S11a between the excited states of Er^{3+} and the valence band of Na_3ZrF_7 host can take place in Na_3ZrF_7:Yb/Er NCs. These successive ET processes will somewhat increase the populations of the $^4I_{13/2}$ state of Er^{3+}, and subsequently lead to the increased populations of $^4F_{9/2}$ of Er^{3+} following the third ET step from the excited Yb^{3+} to Er^{3+} upon 980-nm laser excitation. As a result, the red UCL intensity was observed to be much stronger than the green and violent UCL bands of Er^{3+} in Na_3ZrF_7:Yb/Er NCs. By contrast, such ET processes between the excited Er^{3+} ion and the valence band of host materials cannot occur in $Na_5Zr_2F_{13}$:Yb/Er (0.69 eV) and $Na_7Zr_6F_{31}$:Yb/Er (0.51 eV) NCs due to their much lower VBM energies than that of Na_3ZrF_7:Yb/Er NCs (Figure S11b-c), which reveals that the $^4I_{13/2}$ and $^4F_{9/2}$ states of Er^{3+} in $Na_5Zr_2F_{13}$:Yb/Er and $Na_7Zr_6F_{31}$:Yb/Er can not be populated by additional photons as achieved in Na_3ZrF_7:Yb/Er NCs. This was the main reason why the larger UCL R/G ratio of Er^{3+} was achieved in Na_3ZrF_7:Yb/Er NCs than in their $Na_5Zr_2F_{13}$:Yb/Er and $Na_7Zr_6F_{31}$:Yb/Er counterparts.

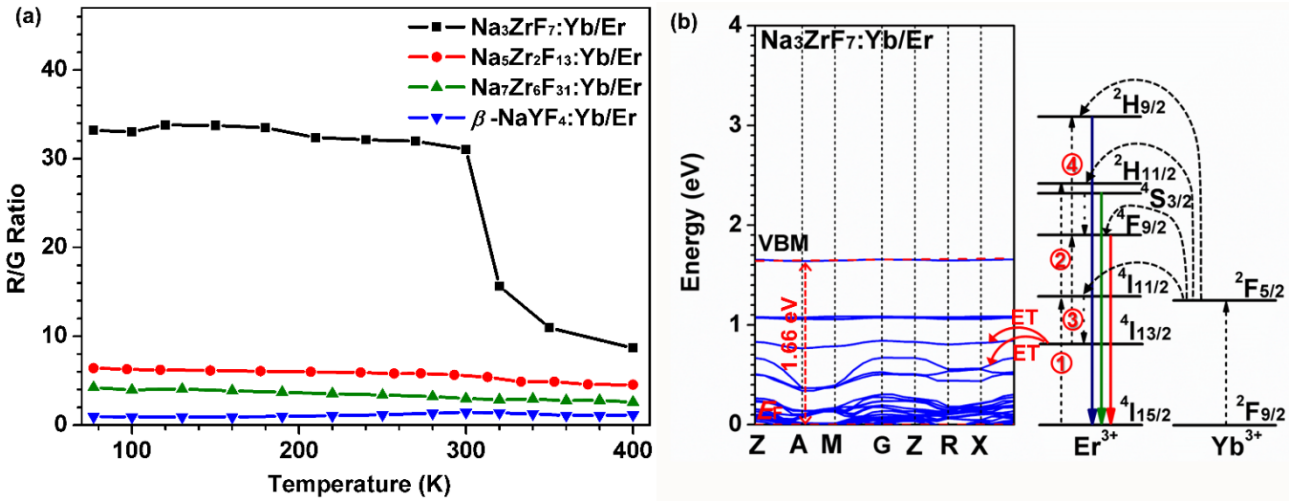

Figure S12. Temperature-dependent UCL intensities for the as-synthesized Na_3ZrF_7:Yb/Er, $Na_5Zr_2F_{13}$:Yb/Er, $Na_7Zr_6F_{31}$:Yb/Er and $NaYF_4$:Yb/Er NCs measured in a temperature range from 77 to 400 K when excited with a 980-nm diode laser at a power density of 30 W cm^{-2}. An abrupt drop in the UCL R/G ratio for the temperature-dependent UCL spectra of Na_3ZrF_7:Yb/Er NCswas detected when measured above 300 K, which was in stark contrast to the cases of $Na_5Zr_2F_{13}$:Yb/Er and $Na_7Zr_6F_{31}$:Yb/Er NCswhose UCL R/G ratios remain essentially unchanged even when heated to 400 K. Note that such abrupt drop in the UCL R/G ratio was also not detected in well-established UCL of Yb/Er co-doped hexagonal-phase $NaYF_4$:Yb/Er NCs (blue in Figure S12a). These results may be caused by the increased probability of energy transfers from the $^4I_{13/2}$ state of Er^{3+} to the sublevels of valence band of Na_3ZrF_7:Yb/Er NCs at high temperature (>300 K) owing to the small energy mismatch (highlighted by red arrows in Figure S12b), which will somewhat decrease the populations of the $^4I_{13/2}$ state of Er^{3+} in Na_3ZrF_7:Yb^{3+}/Er^{3+} NCs and thus result in the decreased UCL R/G ratio above 300 K. By contrast, due to the large energy mismatch between the $^4I_{13/2}$ state of Er^{3+} to the valence band of $Na_5Zr_2F_{13}$:Yb/Er and $Na_7Zr_6F_{31}$:Yb/Er NCs (Figure S11b-c), such temperature-promoted energy transfer processes similar to the case of Na_3ZrF_7:Yb/Er NCs were negligible even at 400 K. As a result, no abrupt drop in the UCL R/G ratio was detected in $Na_5Zr_2F_{13}$:Yb/Er and $Na_7Zr_6F_{31}$:Yb/Er NCs.

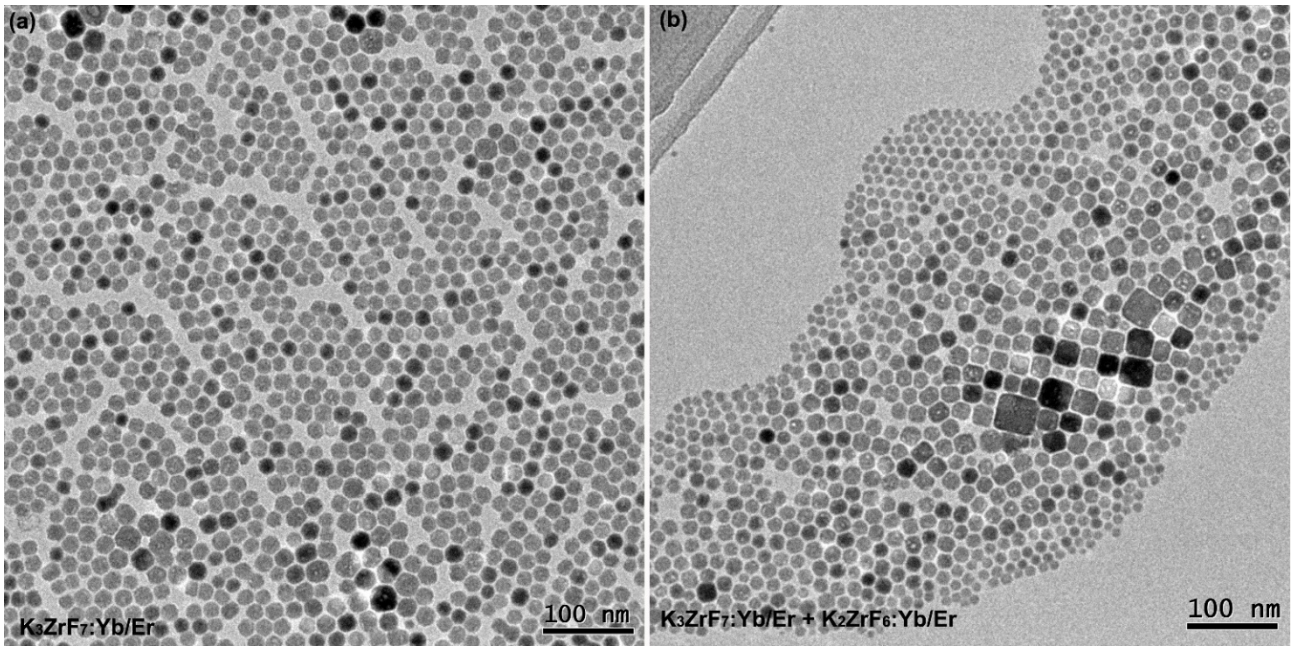

Figure S13. TEM images for the mixed potassium zirconium fluoride NCs with different K_3ZrF_7:Yb/Er and K_2ZrF_6:Yb/Er contents, showing the morphology transformation from a) cubic-phase K_3ZrF_7 to b) the mixed potassium zirconium fluoride NCs of cubic-phase K_3ZrF_7 and monoclinic-phase K_2ZrF_6.

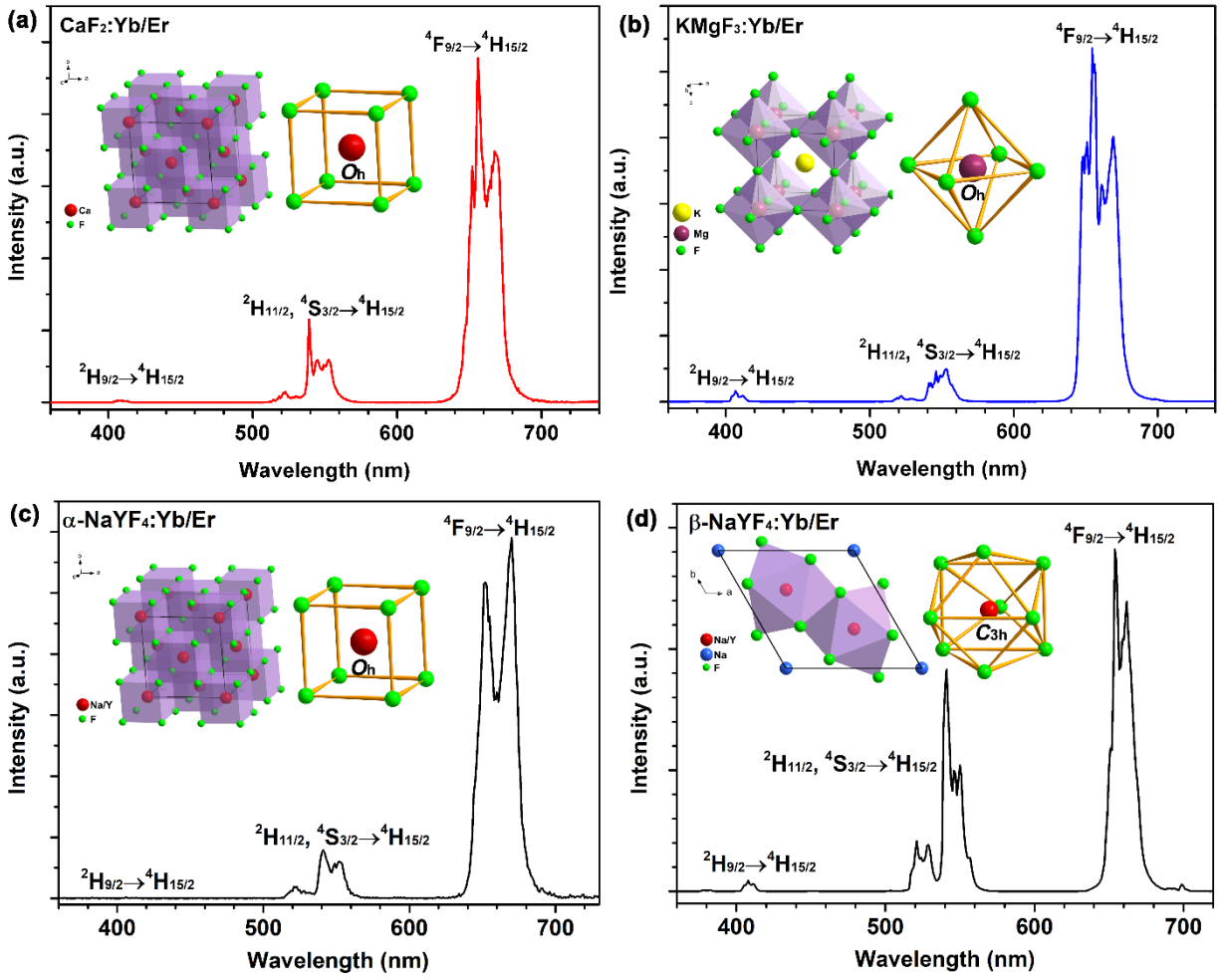

Figure S14. Typical UCL spectra for Yb^{3+}/Er^{3+} (20/2 mol%) co-doped cubic-phase (a) CaF_2 (ICSD No. 41413, space group *F*m-3m), (b) $KMgF_3$ (ICSD No. 40476, space group *P*m-3m) and (c) $NaYF_4$ (JCPDS No. 77-2042, space group *F*m-3m) NCs featuring high-symmetry crystal sublattices of host cations under excitation of 980-nm diode laser at a power density of 30 Wcm^{-2}. For comparison, the well-established UCL spectrum of Yb^{3+}/Er^{3+} (20/2 mol%) co-doped hexagonal-phase $NaYF_4$ NCs (JCPDS No. 28-1192, space group $P6_3/m$) with a low-symmetry crystal sublattices of host cation (Y^{3+}, C_{3h}) was also shown in Figure S14d. The integrated intensities for the green UCL peaks for cubic-phase Yb^{3+}/Er^{3+} co-doped CaF_2, $KMgF_3$ and $NaYF_4$ NCs were observed to be about 3-5 times weaker than their red UCL peaks, which differs markedly from that of hexagonal-phase $NaYF_4$ NCs with comparable red and green UCL intensities. These results further corroborate the possibility and generality to manipulate the UCL through engineering the local structure in diverse Ln^{3+}-doped UCNCs. Namely, the higher symmetry of crystal sublattice of host cation, the larger UCL R/G ratio of the substituted doping Er^{3+} ion in Ln^{3+}-doped inorganic upconversion NCs.

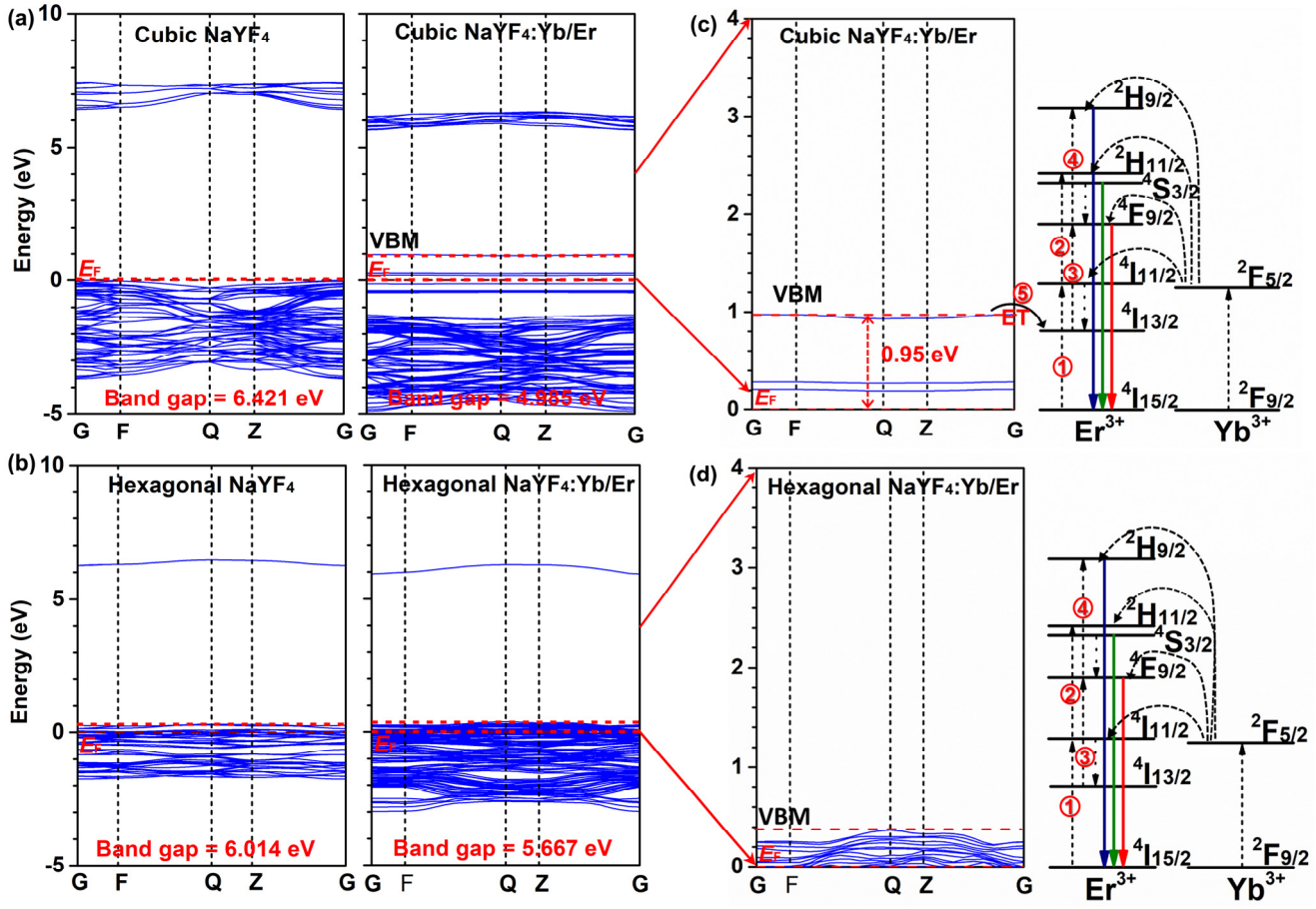

Figure S15. Comparison of DFT-calculated electronic band structures for pure and Yb/Er co-doped (a) cubic-phase and (b) hexagonal-phase $NaYF_4$ NCs, and the proposed energy transfer (ET) mechanisms between the excited Yb^{3+}, Er^{3+} and the valence bands in (c) cubic-phase $NaYF_4$:Yb/Er and (d) hexagonal-phase $NaYF_4$:Yb/Er NCs following excitation with a 980-nm laser. Note that the dashed, dotted, black and colored full arrows represent photon excitation, non-radiative multiphonon relaxation, ET and emission processes, respectively. As shown in Figure S15a-b, the VBM for the cubic-phase $NaYF_4$:Yb/Er NCs was calculated to significantly increase from Fermi level (E_F, 0 eV) to 0.95 eV, while the VBM for the hexagonal-phase $NaYF_4$:Yb/Er NCs kept almost unchanged before and after Yb^{3+}/Er^{3+} doping. These results clearly demonstrate that that the symmetry of crystal lattices of these cubic-phase and hexagonal-phase $NaYF_4$:Yb/Er NCs has significant impact on their repective electronic band structures after Yb^{3+}/Er^{3+} doping, similar to the cases of Yb^{3+}/Er^{3+} co-doped alkaline zirconium fluoride NCs aforementioned (Figure S10). Likewise, such significantly increased VBM (0.95 eV) for cubic-phase $NaYF_4$:Yb/Er NCs can promote the ET beteeen the valence band of the host and excited Er^{3+} ion (Fgiure S15c), which will ultimately lead to the increased UCL R/G ratio in cubic-phase $NaYF_4$:Yb/Er NCs when compared to their hexagonal-phase counterparts.